Phase coexistence and electric-field control of toroidal order in oxide superlattices

A. R. Damodaran[1,2,†], J. D. Clarkson[1,2,†], Z. Hong[3], H. Liu[4], A. K. Yadav[1,2,5], C. T. Nelson[1,6], S.-L. Hsu[1,6], M. R. McCarter[7], K.-D. Park[8], V. Kravtsov[8], A. Farhan[9], Y. Dong[4], Z. Cai[10], H. Zhou[10], P. Aguado-Puente[11,12], P. García-Fernández[13], J. Íñiguez[14], J. Junquera[13], A. Scholl[9], M. B. Raschke[8], L.-Q. Chen[3], D. D. Fong[4], R. Ramesh[1,2,7] and L. W. Martin[1,2]*

Systems that exhibit phase competition, order parameter coexistence, and emergent order parameter topologies constitute a major part of modern condensed-matter physics. Here, by applying a range of characterization techniques, and simulations, we observe that in $PbTiO_3/SrTiO_3$ superlattices all of these effects can be found. By exploring superlattice period-, temperature- and field-dependent evolution of these structures, we observe several new features. First, it is possible to engineer phase coexistence mediated by a first-order phase transition between an emergent, low-temperature vortex phase with electric toroidal order and a high-temperature ferroelectric a_1/a_2 phase. At room temperature, the coexisting vortex and ferroelectric phases form a mesoscale, fibre-textured hierarchical superstructure. The vortex phase possesses an axial polarization, set by the net polarization of the surrounding ferroelectric domains, such that it possesses a multi-order-parameter state and belongs to a class of gyrotropic electrotoroidal compounds. Finally, application of electric fields to this mixed-phase system permits interconversion between the vortex and the ferroelectric phases concomitant with order-of-magnitude changes in piezoelectric and nonlinear optical responses. Our findings suggest new cross-coupled functionalities.

High-temperature superconductivity[1], colossal magnetoresistance[2,3] and multi-ferroism[4–7] (that is, materials simultaneously exhibiting magnetic and ferroelectric order) represent some of the key discoveries of condensed-matter physics in the past few decades. In all cases, emergent phenomena arise from the interplay of spin, charge, orbital and/or lattice degrees of freedom and related coupling that leads to a rich spectrum of competing phases and novel effects[8–10]. Understanding the nature of spontaneous symmetry breaking and ordering in these phases, and the phase transition pathway under applied stimuli is of fundamental significance. At such phase boundaries, there is often the opportunity to induce colossal field-driven effects (for example, colossal magnetoresistance[11,12] in mixed-valent manganites, giant electromechanical responses at morphotropic phase boundaries[13–16] and so on). At the same time, considerable interest has been given to exploring new phases with non-trivial, real-space order parameter topologies and emergent continuous symmetry that can occur at the mesoscale (for example, complex spin textures such as vortices and skyrmions[17–19]).

In the case of ferroelectrics, several theoretical studies[20–24] have proposed complex polarization topologies (reminiscent of rotational spin topologies) in low-dimensional structures. The models have predicted the formation of polarization waves, vortices and so on that can be characterized by an emergent order parameter, a so-called electric toroidal moment ($\mathbf{G} = (1/2V) \int \mathbf{r} \times \mathbf{P}(\mathbf{r}) \, d^3r$; refs 20,22,25). Such toroidal moments can also give rise to a range of novel phenomena (for example, pyrotoroidic, piezotoroidic and so on effects) in response to thermodynamic stimuli. Experimental realization of such structures occurred only recently[26], wherein superlattices of $(PbTiO_3)_n/(SrTiO_3)_n$ ($n \approx 12$–20 unit cells) exhibiting novel polarization-based topologies (namely polarization vortices) were achieved by inducing a competition between electrostatic and strain boundary conditions that inhibit the formation of a homogeneous ferroelectric ground state. The result was nanometre-scale vortex arrays that match the predictions for structures exhibiting an electric toroidal moment.

By exploring superlattice period-, temperature- and field-dependent evolution using phase-field models, second-principle calculations, synchrotron X-ray diffraction, piezoresponse force microscopy (PFM), X-ray photoemission electron microscopy (PEEM)-based linear dichroism, and optical second-harmonic generation (SHG) and SHG nano-imaging, we have discovered that these superlattices exhibit a rich diversity of physical phenomena. Most important is the observation of phase coexistence mediated

[1]Department of Materials Science and Engineering, University of California, Berkeley, California 94720, USA. [2]Materials Sciences Division, Lawrence Berkeley National Laboratory, Berkeley, California 94720, USA. [3]Department of Materials Science and Engineering, Pennsylvania State University, State College, Pennsylvania 16802, USA. [4]Materials Science Division, Argonne National Laboratory, Argonne, Illinois 60439, USA. [5]School of Electrical Engineering and Computer Science, UC Berkeley, Berkeley, California 94720, USA. [6]National Center for Electron Microscopy, Lawrence Berkeley National Laboratory, Berkeley, California 94720, USA. [7]Department of Physics, University of California, Berkeley, Berkeley, California 94720, USA. [8]Department of Physics, Department of Chemistry, and JILA, University of Colorado, Boulder, Colorado 80309, USA. [9]Advanced Light Source, Lawrence Berkeley National Laboratory, Berkeley, California 94720, USA. [10]X-ray Science Division, Argonne National Laboratory, Argonne, Illinois 60439, USA. [11]Centro de Física de Materiales, Universidad del País Vasco, 20018 San Sebastián, Spain. [12]Donostia International Physics Center, 20018 San Sebastián, Spain. [13]Departamento de Ciencias de la Tierra y Física de la Materia Condensada, Universidad de Cantabria, Cantabria Campus Internacional, avenida de los Castros s/n, 39005 Santander, Spain. [14]Materials Research and Technology Department, Luxembourg Institute of Science and Technology (LIST), 5 avenue des Hauts-Fourneaux, L-4362 Esch/Alzette, Luxembourg. [†]These authors contributed equally to this work. *e-mail: lwmartin@berkeley.edu
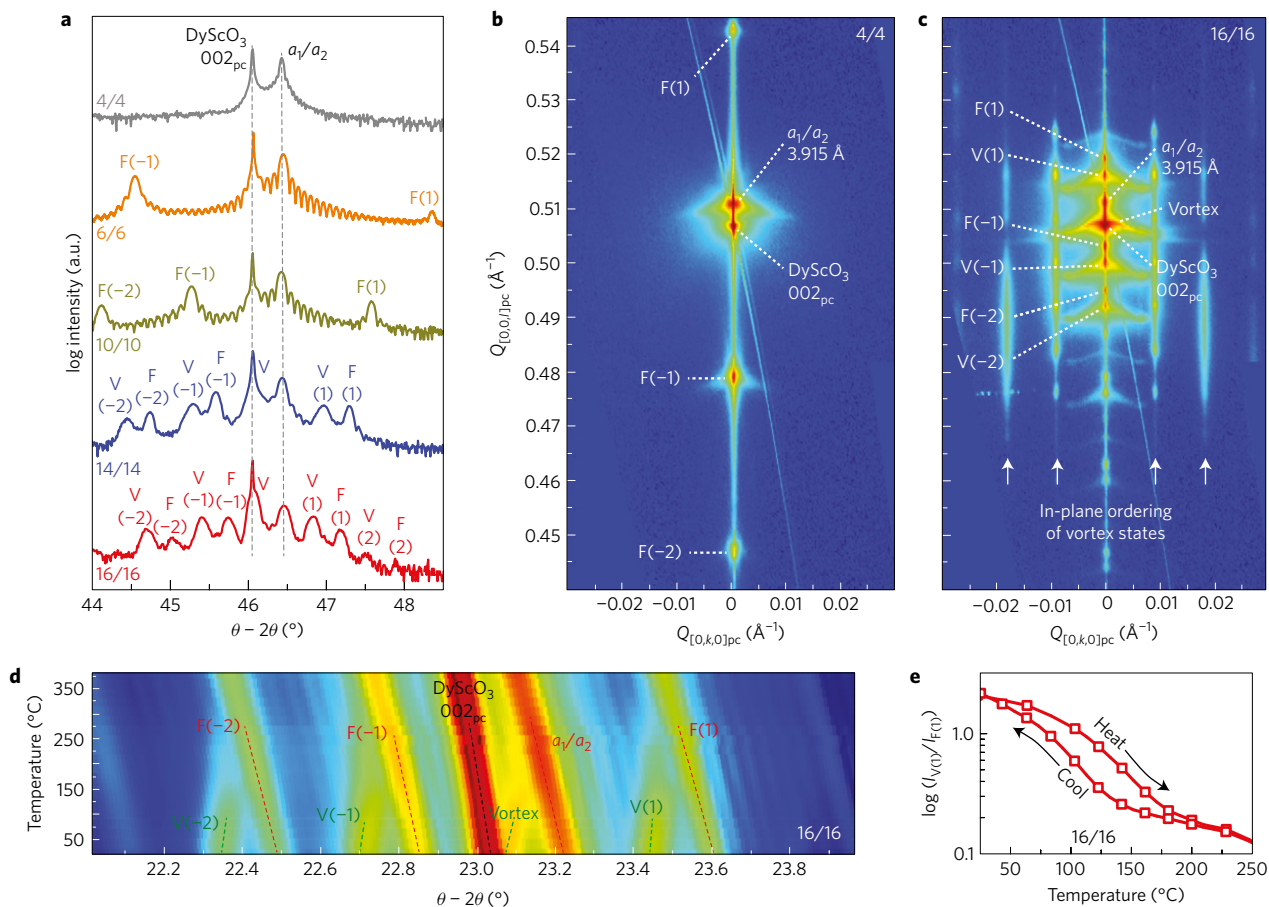
Figure 1 | Structural evolution of ferroelectric and vortex phases with superlattice periodicity. a, High-resolution $\theta - 2\theta$ scans of 100-nm-thick $(PbTiO_3)_n/(SrTiO_3)_n$ superlattices grown on $DyScO_3$ $(001)_{pc}$ substrates for $n = 4, 6, 10, 14$ and 16 (top to bottom, respectively) revealing evolution from a single a_1/a_2 alloy peak and corresponding superlattice peaks at short periodicities to mixed-phase films revealing an extra set of alloy and superlattice peaks corresponding to the vortex (V) phase. **b,c**, Three-dimensional, synchrotron-based symmetric reciprocal space maps about the 002_{pc}-diffraction condition of the $DyScO_3$ substrate containing the in-plane $[010]_{pc}$ and out-of-plane $[001]_{pc}$ confirming (**b**) single a_1/a_2 alloy peak and corresponding superlattice peaks at $n = 4$, and (**c**) mixed-phase coexistence for $n = 16$ showing additional set of alloy and superlattice peaks corresponding to the vortex phase along with the appearance of characteristic satellite peaks corresponding to an in-plane periodicity of ~ 11 nm along the in-plane $[010]_{pc}$.
d, 2D intensity colour-map summarizing temperature-dependent synchrotron X-ray diffraction $\theta - 2\theta$ scans about the 002_{pc}-diffraction condition of the $DyScO_3$ substrate, and **e**, a plot of the ratio of diffracted beam intensity from a vortex superlattice peak ($I_{V(1)}$) to the a_1/a_2 superlattice peak ($I_{F(1)}$) revealing hysteresis indicative of a first-order phase transition from the vortex phase to the a_1/a_2 phase at $\sim 200\,^{\circ}C$.

by a first-order phase transition between an emergent, low-temperature vortex phase with electric toroidal order and a high-temperature ferroelectric a_1/a_2 phase. At room temperature, the coexisting vortex and ferroelectric phases spontaneously assemble in a mesoscale, fibre-textured, hierarchical superstructure. The vortex phase is further found to possess an axial polarization (P_{ax}) that is set by the net polarization of the surrounding ferroelectric domains such that it possesses a multi-order-parameter state and belongs to a class of potentially chiral and naturally gyrotropic electrotoroidal compounds[22,25]. Finally, application of electric fields to this mixed-phase system results in deterministic interconversion between the vortex and the ferroelectric phases concomitant with order-of-magnitude changes in piezoelectric and nonlinear optical responses and promise for new cross-coupled functionalities.

$(PbTiO_3)_n/(SrTiO_3)_n$ superlattices ($n = 4, 6, \ldots, 16$) were synthesized on 5 nm $SrRuO_3$-buffered $DyScO_3$ (110) ($(001)_{pc}$, where pc indicates pseudocubic indices) substrates using established procedures (Methods)[26]. X-ray diffraction $\theta - 2\theta$ studies about the 002_{pc}-diffraction condition of the $DyScO_3$ substrate reveal an interesting evolution in structure with superlattice periodicity (Fig. 1a). Superlattices with $n = 4$–10 reveal a single alloy film peak ($c \approx 3.915$ Å) along with first- and higher-order superlattice reflections (labelled

as F ($\pm m$)). Synchrotron-based three-dimensional (3D)-reciprocal space mapping (RSM) (Supplementary Fig. 1) and high-resolution PFM (Supplementary Fig. 2a) studies show that the single alloy film peak corresponds to a phase with in-plane polarized ferroelectric a_1/a_2 stripe domains running along the $[110]_{pc}$ (henceforth referred to as the a_1/a_2 phase). Moreover, the a_1/a_2 domain width progressively reduces with increasing superlattice periodicity (Supplementary Fig. 2c); indicative of a thickness regime where interface effects dominate and Kittel's law scaling is invalid[27,28].

On transitioning from short- to intermediate-period superlattices (that is, $n = 12$–18), where interface effects are less dominant, the a domain size decreases to its lowest value (~ 6 nm). In addition to the diffraction peaks corresponding to the a_1/a_2 phase, X-ray $\theta - 2\theta$ scans also reveal an extra set of alloy ($c \approx 3.944$ Å, labelled V) and superlattice (labelled V ($\pm m$)) peaks indicative of a new phase (Fig. 1a); thus suggesting the possibility of an emergent mixed-phase structure. Additional insights into this new phase are obtained from 3D-RSM studies (Supplementary Fig. 3) and, for brevity, we compare a planar section of the 3D-RSM about the 002_{pc}-diffraction condition for the $n = 4$ (Fig. 1b) and $n = 16$ (Fig. 1c) superlattices. Consistent with the $\theta - 2\theta$ scans, the $n = 16$ superlattices show extra peaks corresponding to the new phase (V) and associated V ($\pm m$)

superlattice peaks along the out-of-plane $[001]_{pc}$. The new phase (V) is also found to produce satellite peaks (marked by arrows) along the in-plane $[010]_{pc}$ corresponding to an ordering of ~11 nm; characteristic of the recently identified vortex phase[26]. The emergent vortex structures in these intermediate-period superlattices are also confirmed via ferroelectric polarization mapping of an $n=14$ superlattice using high-resolution scanning transmission electron microscopy (Supplementary Fig. 4). This is consistent with phase-field studies[26,29] that predict a crossover of energies for vortex and ferroelectric a_1/a_2 phases at an intermediate periodicity regime ($n\approx10$ unit cells). These studies reveal that as the superlattice periodicity is varied, the system enters a regime of phase competition wherein phases with ferroelectric and electric toroidal order coexist.

To further understand the nature of such mixed-phase coexistence, temperature-dependent X-ray diffraction $\theta-2\theta$ studies about the 002_{pc}-diffraction condition of the $DyScO_3$ substrate were completed to probe the evolution of the various phases (data for selected temperatures, Supplementary Fig. 5). A 2D-colour-map showing the diffracted beam intensity as a function of 2θ and temperature reveals a continuous decrease (increase) in the intensity of peaks corresponding to the vortex (a_1/a_2) phase revealing a direct phase transformation pathway from the mixed-phase structure to a purely ferroelectric a_1/a_2 phase at $\sim200\,^\circ$C (Fig. 1d). A subsequent transition from the a_1/a_2 phase to the paraelectric phase occurs at a temperature of $\sim325\,^\circ$C (Supplementary Fig. 6). On returning to room temperature, the mixed-phase structure re-emerges with a thermal hysteresis indicating a first-order phase transition between the ferroelectric a_1/a_2 and vortex states (Fig. 1e).

The nanoscale phase separation between ferroelectric and vortex phases in intermediate-period superlattices also manifests itself in PFM (Fig. 2a) as a complex pattern that is dramatically different from the a_1/a_2 twin structure (for example, see the $n=4$ superlattices; Supplementary Fig. 2a). The lateral piezoresponse image for an $n=16$ superlattice reveals stripe-like order in which alternating stripes exhibit high (chequered white and black) and low or zero (brown) piezoresponse with a periodicity of ~300 nm along the $[100]_{pc}$. The high-response regions are the ferroelectric a_1/a_2 phase that exhibits a net polarization along the in-plane $\langle110\rangle_{pc}$ (from vector PFM studies, Supplementary Fig. 7) and individual domain widths of only 6–7 nm (from X-ray studies, Fig. 1c) and the low-response regions are the vortex structures. This is further confirmed from height modulation of the sample surface since the difference in the unit cell lattice parameters between the vortex ($c=3.94$ Å) and a_1/a_2 ($c=3.915$ Å) phases gives rise to systematic variations in the surface topography (Fig. 2b) and correlated changes in the lateral piezoresponse amplitude (Fig. 2c). This correlation is highlighted by line traces along a terrace step of the film (dashed lines, Fig. 2b,c) that shows opposite trends in height (green, Fig. 2d) and lateral piezoresponse amplitude (red, Fig. 2d). Ultimately, these data indicate that at room temperature, the coexisting vortex and ferroelectric phases spontaneously assemble in a mesoscale, fibre-textured, hierarchical superstructure.

To understand the microscopic details of how the ferroelectric phase evolves into the vortex phase, we first focus on a single $PbTiO_3$ layer within the superlattice near the phase boundary as extracted from phase-field models (Fig. 3a). As expected, the a_1/a_2 domains (labelled FE (a_1/a_2) wherein the colour scale shows the polarization component along the $[100]_{pc}$) exhibit uniform polarization along the $[100]_{pc}$ and $[010]_{pc}$ resulting in a net polarization along the $[110]_{pc}$ (white arrow, Fig. 3a). As one transitions into the vortex phase (labelled Vortex wherein the colour scale corresponds to the magnitude of $\nabla\times P$), the polarization evolves into polarization vortices with axes aligned along the $[100]_{pc}$. More insight into the nature of this phase boundary can be obtained by tracking the evolution of the polarization components ($\langle P_{100}\rangle$, $\langle P_{010}\rangle$ and $\langle P_{001}\rangle$) as well as the magnitude of the axial electric toroidal
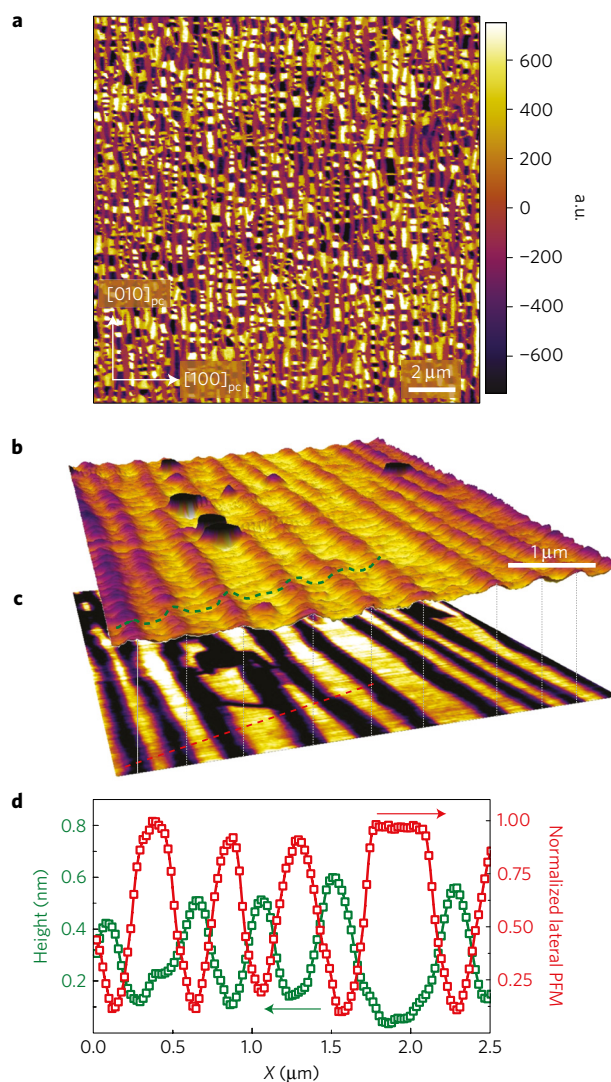
Figure 2 | Unravelling the nanoscale distribution of ferroelectric and vortex phases. a, Lateral piezoresponse image for an $n=16$ superlattice revealing stripe-like order in which alternating stripes exhibit high (chequered white and black) and low or zero (brown) piezoresponse with a periodicity of ~300 nm along the $[010]_{pc}$. Correlation of **b**, variations in the surface topography to **c**, changes in the lateral piezoresponse amplitude in tandem with insights from X-ray diffraction studies confirm that the vortex phase corresponds to protruding features in surface topography with low piezoresponse while the a_1/a_2 phase is recessed in topography with large lateral piezoresponse. **d**, A line trace across the topography (green-dashed line) and lateral piezoresponse images (red-dashed line) revealing opposite and dramatic modulations in surface topography and lateral piezoresponse between the a_1/a_2 and the vortex phases.

moment ($\langle|\mathbf{G}|\rangle$, averaged across the section) as one transitions from the ferroelectric to vortex structure (Fig. 3b). Starting with the ferroelectric phase, we observe constant in-plane polarization components and near-zero $\langle|\mathbf{G}|\rangle$. The transition to the vortex phase occurs over ~20 unit cells and is characterized by complex polarization rotation pathways (reminiscent of Bloch- and Neel-like walls in ferromagnets) along with a continuously increasing $\langle|\mathbf{G}|\rangle$ that eventually saturates to a large value of 0.2 e Å^{-1} that arises from the continuous rotation of polarization within the vortex structures (blue box, Fig. 3a and in colour-maps of the polarization components P_{001} (Fig. 3c), P_{010} (Fig. 3d) and P_{100} (Fig. 3e) for the same section). We also note that the clockwise and anticlockwise
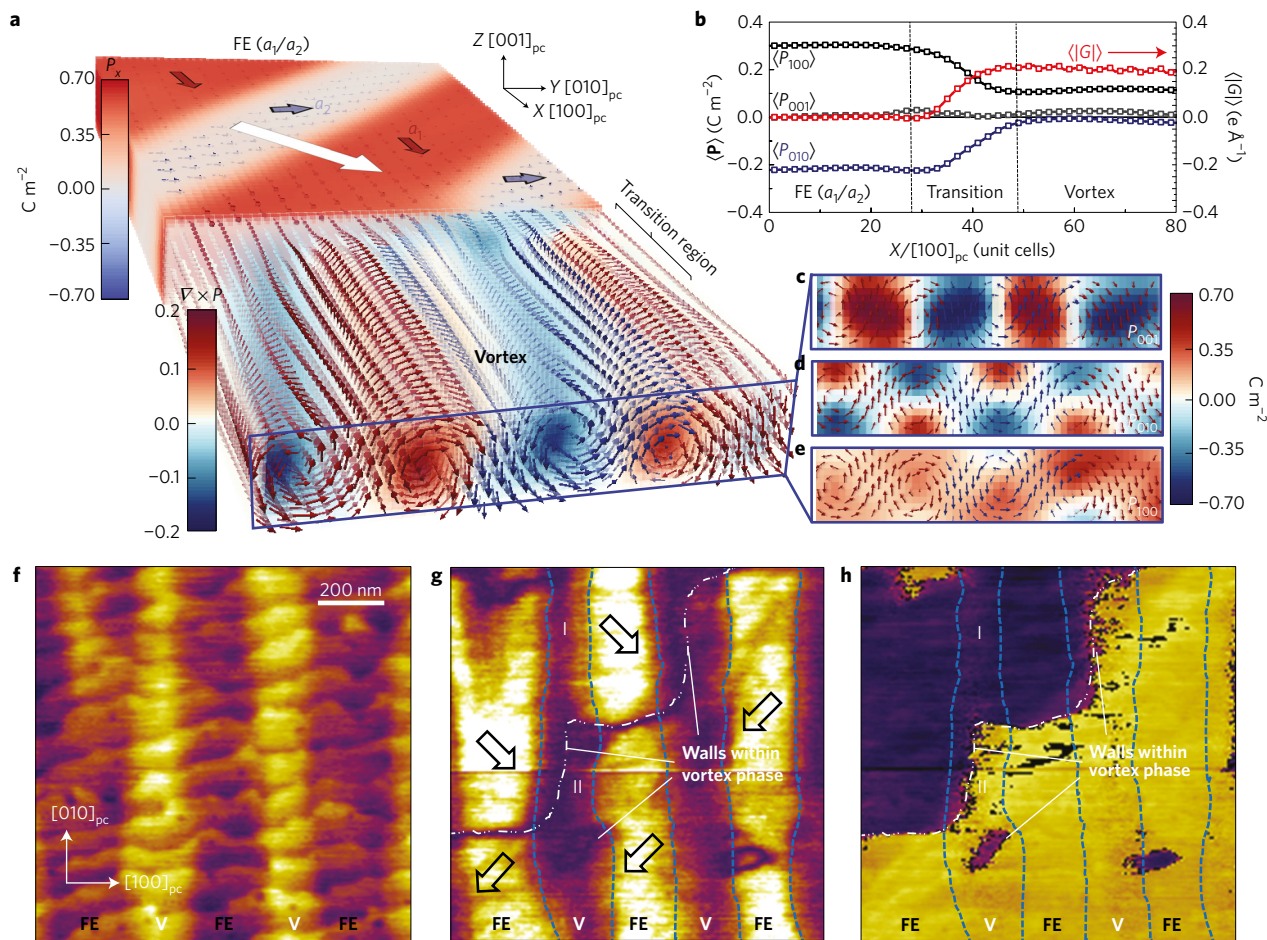
Figure 3 | Exploring the phase boundary between a_1/a_2 and vortex phases. a, A zoom-in of the phase-field calculation focusing on a single PbTiO$_3$ layer near the phase boundary and revealing that the ferroelectric a_1/a_2 superdomain (labelled FE(a_1/a_2), colour scale showing polarization component along $[100]_{pc}$ or the X-direction) smoothly transitions to the vortex phase (labelled Vortex, colour scale corresponding to magnitude of $\nabla \times P$) comprising of alternating clockwise and anticlockwise polarization vortices. **b**, Plot showing the spatially averaged ferroelectric polarization components ($\langle P_{001} \rangle$, $\langle P_{010} \rangle$ and $\langle P_{100} \rangle$) and the averaged magnitude of the axial electrical toroidal moment ($\langle |\mathbf{G}| \rangle$) as one traverses across the phase boundary along [100] from the ferroelectric to the vortex phase. **c–e** are colour-maps showing the spatial distribution of the (**c**) P_{001}, (**d**) P_{010} and (**e**) P_{100} components for a cross-section (blue box, **a**) of the vortex phase and highlight the coexistence of toroidization and an axial component ($P_{100} \approx 0.1$ C m^{-2}) of polarization, the direction of which is related to polarization in the adjacent a_1/a_2 phase. **f–h**, Lateral piezoresponse force studies showing (**f**) topography, (**g**) lateral amplitude, and (**h**) lateral phase revealing the nanoscale distribution of a_1/a_2 and vortex phases, and highlighting the presence of domain-wall-like features within the vortex phase that are indicative of axial polarization components.

vortices are arranged in an alternating fashion, such that the toroidal moment **G** periodically switches direction (akin to what has been called an antiferrotoroidal phase)[21].

Also notable is that while the spatial averages of the non-axial polarization components ($\langle P_{001} \rangle$, $\langle P_{010} \rangle$) go to zero within the vortex phase, a sizable axial component ($\langle P_{100} \rangle \approx 0.1$ C m^{-2}) is observed (Fig. 3b); the direction of which is related to the component of net polarization in the adjacent ferroelectric phase. In turn, this produces a screw-like character to the vortex phase and suggests that the vortex structure is characterized by a multi-order-parameter state consisting of axial ferroelectric polarization that coexists with **G**. This is also observed in second-principles calculations (Supplementary Fig. 8) for an $n = 14$ superlattice (Methods and Supplementary Fig. 9) and is consistent with previous predictions for low-dimensional ferroelectrics[23,30–33]. Such axial polarization can be experimentally observed by focusing on a region of phase coexistence (that is, alternating ferroelectric a_1/a_2 and vortex stripes, Fig. 3f). Using PFM, it is again observed that the amplitude of the piezoresponse (Fig. 3g) is higher in the ferroelectric a_1/a_2 regions than in the vortex regions, which, along with the topography, allows for clear demarcation of the regions. The phase

of the piezoresponse (Fig. 3h) shows two contrasts across the same area. By combining the amplitude and phase data, the fact that the cantilever axis is aligned along the $[010]_{pc}$, and our understanding of the a_1/a_2 structure, the net in-plane polarization for each area can be extracted (arrows, Fig. 3g). Consistent with the phase-field predictions, the axial polarization component of the vortex phase is set by the direction of the polarization in the adjacent a_1/a_2 stripe (for example, region I, Fig. 3g,h). There are situations, however, when adjacent a_1/a_2 stripes on either side of a vortex region possess opposite net in-plane polarization, and in this case we observe an inversion of the lateral phase signal in the vortex region indicative of a 'domain-wall-like' feature (for example, region II, Fig. 3g,h). Either way, both the phase-field models and PFM data suggest that the vortex structures possess an axial component of polarization that is correlated with the polarization in the surrounding ferroelectric phase.

The presence of this axial polarization component is interesting because it suggests the formation of a multi-order-parameter state. In turn, electric-field control of toroidal order is of great interest because it offers the potential for new cross-coupled functions[20–24]. To explore this concept, the time-dependent evolution of both the

vortex and a_1/a_2 regions of a mixed-phase structure was explored under an applied out-of-plane voltage (15 V) using phase-field models. Specifically we have collected the evolution of energy and polarization under bias (1,500 time steps) and during relaxation after the bias is turned off (16,000 time steps; where each time step is ≈40 fs). After turning on the voltage, the various energies (green and red data, respectively, for the vortex and a_1/a_2 phases; Fig. 4a) and polarization states (Fig. 4b–d) are observed to evolve. Starting from the as-grown, mixed-phase state (bias time step 1, Fig. 4a,b), the out-of-plane voltage drives a rotation of the polarization towards the field direction reducing the electric energy of the system (bias time steps ∼1–100, Fig. 4a). Within the a_1/a_2 regions, this corresponds to a rotation of the polarization in the applied field direction (not shown) and within the vortex regions (Fig. 4c), the polarization in the direction of the applied voltage is found to be enhanced and that opposite to the voltage is reduced thereby quenching the vortex structure. Both the a_1/a_2 and the vortex structures ultimately trend to the same final state, a uniformly poled, monoclinic state with large out-of-plane polarization ($\sim$70 μC cm^{-2}, time steps >200, Fig. 4a,d). We note that this evolution is almost entirely driven by a reduction in the electrical energy that overcomes barriers in the Landau and elastic energies to align the polarization in the field direction.

After turning off the applied bias and allowing the system to relax, again a complex evolution of the energies (Fig. 4e) and polarization states (Fig. 4f–h) is observed wherein the entire sample relaxes in a similar fashion. Immediately after turning off the applied bias (time step 1, Fig. 4e), there is a large jump in the electric energy driven by depolarization effects that destabilizes the out-of-plane polarization. In turn, there is a rapid reduction in the electric energy and a corresponding increase in the Landau energy of the system (time steps 1–200, Fig. 4e) due to a reduction of the magnitude of the polarization (from $\sim$70 to 35 μC cm^{-2}) in the out-of-plane direction. This marks the beginning of a series of events driven by a competition between Landau and elastic energies wherein fast changes in the polarization (that is, the Landau energy) are counteracted by slow changes in the elastic energy as it attempts to reach a new equilibrium (time steps 200–8,000, Fig. 4e). In this range, the Landau energy first begins to dominate and works to restore the total polarization by driving the polarization to increase in the in-plane direction resulting in a fully in-plane polarized monodomain structure (by time step 200–300, Fig. 4e). This in-plane polarized phase, however, forms at the expense of enhanced elastic energy and effectively launches an elastic shockwave that drives twinning in the in-plane polarized phase to create an a_1/a_2-like structure (by time step 3,000–4,000, Fig. 4e,f). At this point, the system must activate other means to reach equilibrium since it cannot be accomplished with the Landau and elastic energies alone. Thus, small increases in the electric and gradient energies (corresponding to the introduction of a wave-like instability; time step ∼8,000, Fig. 4e,g) break the oscillatory nature of the Landau and elastic energy variations and drive the formation of the vortex phase across the entire sample (time step 16,000, Fig. 4e,h). Once this phase is formed, no further evolution is observed. Thus, from phase-field simulations, it appears that there is a pathway—albeit a complex one—by which we can not only manipulate the vortex structure, but deterministically control the relative fraction of vortex and a_1/a_2 phases with d.c. electric fields thus making possible effective cross-control of ferroelectric and electric toroidal order that could give rise to a rich spectrum of effects.

To realize this predicted electric-field control of the multi-order-parameter state, we focus on an $n = 16$ superlattice and explore electric-field evolution of the phases under applied d.c. electric fields using PFM. Beginning with an as-grown superlattice in the mixed-phase form (Fig. 5a), application of a positive electrical bias (via a scanning probe tip within the orange box, Fig. 5a) results in the
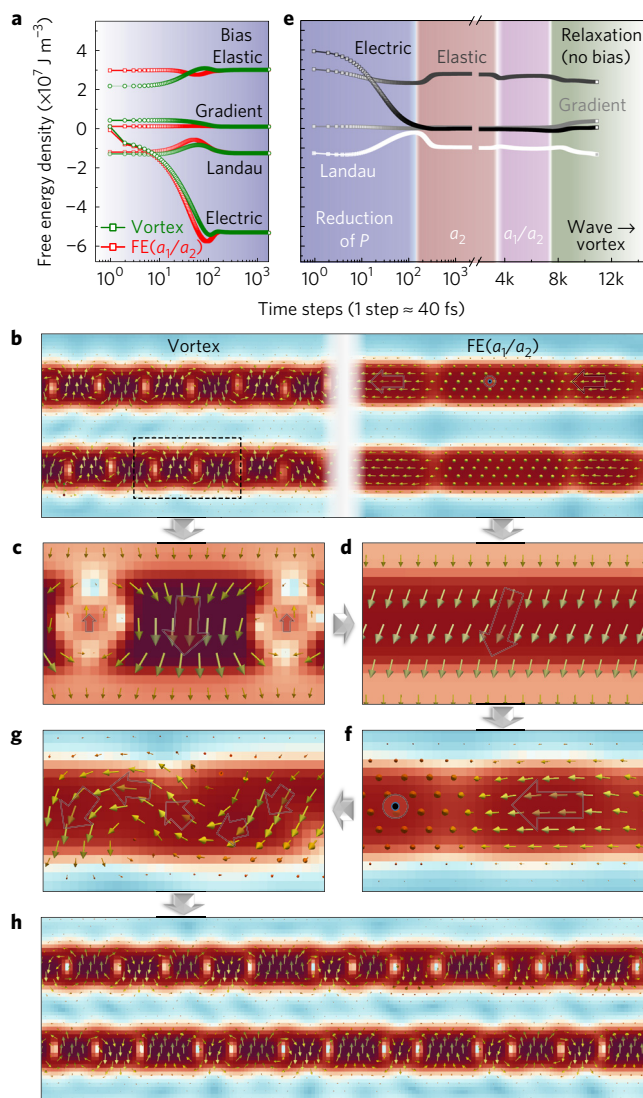

Figure 4 | Phase-field studies of electric-field control of ferroelectric and vortex phases. a, Time-dependent evolution (wherein each time step is ≈40 fs) of energy components of vortex (green data) and a_1/a_2 (red data) regions of a mixed-phase superlattice film under an applied out-of-plane bias (15 V). **b–d**, Simulation cross-sections of the (**b**) as-grown, mixed-phase state, (**c**) the vortex phase (time step 100) under applied bias, and (**d**) the uniform, monoclinic polarization state with out-of-plane polarization component ($\sim$70 μC cm^{-2}) (time step 1,500) for both the vortex and a_1/a_2 phases. After turning off the applied bias and allowing the sample to relax, **e**, the energies evolve in a complex manner. Simulation cross-sections reveal that all areas evolve in the same manner wherein the uniformly polarized state first undergoes **f**, lattice twinning to form an in-plane polarized a_1/a_2-like structure (time step 4,500). From there, the system evolves to **g**, a wave-like instability (time step 8,000) and finally, **h**, reaches a new equilibrium state wherein the entire samples is vortex in nature (time step 16,000).

mixed-phase structure being converted to one with a uniformly low piezoresponse corresponding to the vortex state (Fig. 5b). Similar effects are observed following application of negative bias, which can also give rise to conversion to pure vortex phase (Supplementary Fig. 9). Within this pure vortex region, subsequent application of a negative electrical bias to selected locations (blue lines, Fig. 5a) restores the region back into a mixed-phase structure with similar stripe-like features to the as-grown superlattice (Fig. 5c). Closer inspection reveals that, after applying the negative bias to the tip,
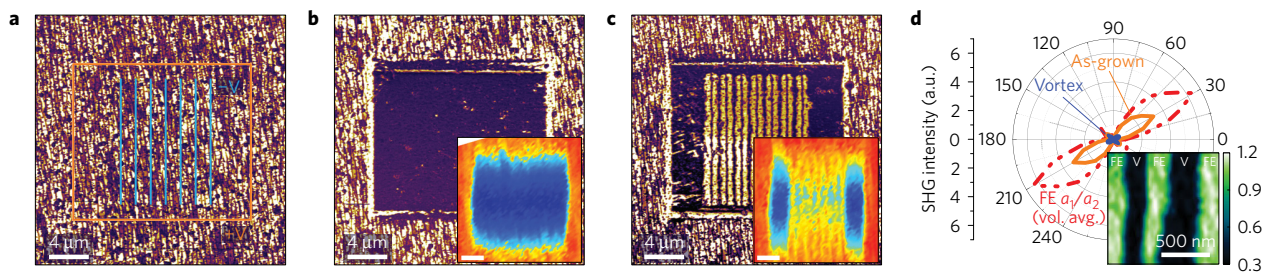
Figure 5 | Reversible electric-field control of ferroelectric and vortex phases. Lateral piezoresponse amplitude images for an $n = 16$ superlattice showing the **a**, as-grown mixed-phase structure, **b**, the conversion to a uniformly low-piezoresponse state corresponding to the vortex phase, as confirmed by nanodiffraction studies showing the intensity of the a_1/a_2 002_{pc}-diffraction peak (inset), following application of a positive 15 V bias and, **c**, reversal of portions of region back into a mixed-phase structure, again confirmed by nanodiffraction studies (inset), following application of a negative 15 V bias. **d**, SHG polar plots obtained from regions with the as-grown mixed-phase structure (orange), the electrically poled pure vortex structure (blue), and that of the volume normalized signal from the a_1/a_2 phase (red-dashed) revealing a large SHG intensity change after transitioning to the vortex phase. The inset shows SHG nano-imaging of the corresponding domain texture with signal contrast between the ferroelectric and vortex regions.

the regions directly under the tip have contrast consistent with the low piezoelectric response of the vortex phase and only adjacent to these written lines (where the in-plane fields from the tip are the strongest) can the high response consistent with the a_1/a_2 phase be observed (Supplementary Fig. 10). This change in phase structure is confirmed via synchrotron X-ray nanodiffraction studies (spatial resolution of ~200 nm, inset of Fig. 5b,c and Supplementary Fig. 11) and PEEM-based X-ray linear dichroism studies (spatial resolution of 30 nm, Supplementary Fig. 12) that provide structural and spectroscopic confirmation, respectively, of the proposed electric-field-induced manipulation of phases. Such reversible electric-field control of the vortex and ferroelectric phases is indicative of a strong coupling between the ferroelectric polarization and electric toroidal moment, the potential for interconversion using a variety of stimuli, and highlights the possibility to control function by tuning the phase fractions. For instance, the SHG response from the as-grown regions (orange data, Fig. 5d) is found to be consistent with that observed for the purely ferroelectric a_1/a_2 phase in a single-layer PbTiO$_3$ film (Supplementary Fig. 13). The ability to electrically switch to a purely vortex state results in a strong reduction of the second-harmonic intensity (blue data, Fig. 5d). In turn, realizing that the presence of the vortex phase results in a reduction of SHG intensity and by normalizing the as-grown signal based on the volume of the two phases, we estimate nearly an order of magnitude reduction in the SHG signal in the vortex phase as compared with the ferroelectric phase. Such effects are also resolved at the nanoscale in near-field SHG nano-imaging (inset, Fig. 5d) obtained using shear-force atomic force microscopy-based scanning near-field optical microscopy (Methods) where the ferroelectric and vortex regions provide alternating strong and weak signals, respectively.

All told, these observations have broad-ranging implications for a range of novel physical phenomena and next-generation applications. First, the establishment of a true electric toroidal moment is important since such structures have not been widely observed experimentally. Second, the demonstrated coexistence and reversible electric-field control of ferroelectric and electric toroidal order provides for a number of novel opportunities for applications. In the simplest form, the ability to 'turn-off' ferroelectric response via conversion to the vortex phase allows for large tunability and susceptibilities. Potentially more interesting is the possibility to both explore and, ultimately, utilize the nature of emergent phenomena made possible by the presence of the electric toroidal moment including electrotoroidic, piezotoroidic and pyrotoroidic susceptibilities; something that has not been possible to date. Finally, the vortex structures themselves also hold tremendous potential for other properties including emergent chirality derived from the screw-like nature of the vortex that could enable electrically switchable optical rotation and dichroism[22]. In fact, it has been

shown that the electric-field derivative of the electric toroidal moment[22,25] is related to the imaginary part of the magnetoelectric susceptibility, and thus can allow for electric-field control of natural optical activity[22]. Ultimately, this work represents an important milestone towards the utilization of complex electrical polarization topologies for next-generation applications.

In summary, this work has demonstrated the possibility to control and engineer phase coexistence between an emergent vortex phase with electric toroidal order and a ferroelectric a_1/a_2 phase. This phase coexistence also exhibits classical temperature-dependence (that is, a first-order phase transformation and hysteretic behaviour) and spontaneous self-assembly into a mesoscale, fibre-textured, hierarchical superstructure at room temperature. Closer inspection of the emergent vortex phase reveals an axial polarization, set by the net polarization of the surrounding ferroelectric domains, suggesting a novel multi-order-parameter state belonging to a class of electrotoroidal phases that are potentially chiral and naturally gyrotropic. In turn, application of electric fields to this mixed-phase system results in deterministic interconversion between the vortex and the ferroelectric phases with associated order-of-magnitude changes in piezoelectric and nonlinear optical response thus demonstrating the potential for novel cross-coupled functionalities.

Methods

Methods, including statements of data availability and any associated accession codes and references, are available in the online version of this paper.

References

1. Dagotto, E. Correlated electrons in high-temperature superconductors. *Rev. Mod. Phys.* **66,** 763–840 (1994).
2. Tokura, Y. & Tomioka, Y. Colossal magnetoresistive manganites. *J. Magn. Magn. Mater.* **200,** 1–23 (1999).
3. Dagotto, E. *Nanoscale Phase Separation and Colossal Magnetoresistance* (Springer, 2003).
4. Dawber, M., Rabe, K. M. & Scott, J. F. Physics of thin-film ferroelectric oxides. *Rev. Mod. Phys.* **77,** 1083–1130 (2005).
5. Manfred, F. Revival of the magnetoelectric effect. *J. Phys. D* **38,** R123 (2005).
6. Ramesh, R. & Spaldin, N. A. Multiferroics: progress and prospects in thin films. *Nat. Mater.* **6,** 21–29 (2007).
7. Cheong, S.-W. & Mostovoy, M. Multiferroics: a magnetic twist for ferroelectricity. *Nat. Mater.* **6,** 13–20 (2007).
8. Tokura, Y. & Nagaosa, N. Orbital physics in transition-metal oxides. *Science* **288,** 462–468 (2000).
9. Imada, M., Fujimori, A. & Tokura, Y. Metal–insulator transitions. *Rev. Mod. Phys.* **70,** 1039–1263 (1998).

10. Zubko, P., Gariglio, S., Gabay, M., Ghosez, P. & Triscone, J.-M. Interface physics in complex oxide heterostructures. *Annu. Rev. Condens. Matter Phys.* **2**, 141–165 (2011).

11. Jin, S. *et al*. Thousandfold change in resistivity in magnetoresistive La–Ca–Mn–O films. *Science* **264**, 413–415 (1994).

12. Uehara, M., Mori, S., Chen, C. H. & Cheong, S. W. Percolative phase separation underlies colossal magnetoresistance in mixed-valent manganites. *Nature* **399**, 560–563 (1999).

13. Noheda, B. & Cox, D. E. Bridging phases at the morphotropic boundaries of lead oxide solid solutions. *Phase Transit.* **79**, 5–20 (2006).

14. Jaffe, B., Cook, W. R. & Jaffe, H. *Piezoelectric Ceramics* (Academic, 1971).

15. Choi, S. W., Shrout, R. T. R., Jang, S. J. & Bhalla, A. S. Dielectric and pyroelectric properties in the $Pb(Mg_{1/3}Nb_{2/3})O_3$-$PbTiO_3$ system. *Ferroelectrics* **100**, 29–38 (1989).

16. Saito, Y. *et al*. Lead-free piezoceramics. *Nature* **432**, 84–87 (2004).

17. Roszler, U. K., Bogdanov, A. N. & Pfleiderer, C. Spontaneous skyrmion ground states in magnetic metals. *Nature* **442**, 797–801 (2006).

18. Mühlbauer, S. *et al*. Skyrmion lattice in a chiral magnet. *Science* **323**, 915–919 (2009).

19. Yu, X. Z. *et al*. Real-space observation of a two-dimensional skyrmion crystal. *Nature* **465**, 901–904 (2010).

20. Naumov, I. I., Bellaiche, L. & Fu, H. Unusual phase transitions in ferroelectric nanodisks and nanorods. *Nature* **432**, 737–740 (2004).

21. Prosandeev, S., Ponomareva, I., Naumov, I., Kornev, I. & Bellaiche, L. Original properties of dipole vortices in zero-dimensional ferroelectrics. *J. Phys. Condens. Matter* **20**, 193201 (2008).

22. Prosandeev, S. *et al*. Natural optical activity and its control by electric field in electrotoroidic systems. *Phys. Rev. B* **87**, 195111 (2013).

23. Chen, W. J., Zheng, Y., Wang, B. & Liu, J. Y. Coexistence of toroidal and polar domains in ferroelectric systems: a strategy for switching ferroelectric vortex. *J. Appl. Phys.* **115**, 214106 (2014).

24. Chen, W. J., Zheng, Y. & Wang, B. Large and tunable polar-toroidal coupling in ferroelectric composite nanowires toward superior electromechanical responses. *Sci. Rep.* **5**, 11165 (2015).

25. Hans, S. Some symmetry aspects of ferroics and single phase multiferroics. *J. Phys. Condens. Matter* **20**, 434201 (2008).

26. Yadav, A. K. *et al*. Observation of polar vortices in oxide superlattices. *Nature* **530**, 198–201 (2016).

27. Pertsev, N. A. & Zembilgotov, A. G. Energetics and geometry of 90° domain structures in epitaxial ferroelectric and ferroelastic films. *J. Appl. Phys.* **78**, 6170–6180 (1995).

28. Catalan, G., Seidel, J., Ramesh, R. & Scott, J. F. Domain wall nanoelectronics. *Rev. Mod. Phys.* **84**, 119–156 (2012).

29. Hong, Z. *et al*. Stability of polar vortex lattice in ferroelectric superlattices. *Nano Lett.* **17**, 2246–2252 (2017).

30. Prosandeev, S., Ponomareva, I., Kornev, I., Naumov, I. & Bellaiche, L. Controlling toroidal moment by means of an inhomogeneous static field: an *ab initio* study. *Phys. Rev. Lett.* **96**, 237601 (2006).

31. Naumov, I. & Fu, H. Vortex-to-polarization phase transformation path in ferroelectric $Pb(ZrTi)O_3$ nanoparticles. *Phys. Rev. Lett.* **98**, 077603 (2007).

32. Naumov, I. & Bratkovsky, A. M. Unusual polarization patterns in flat epitaxial ferroelectric nanoparticles. *Phys. Rev. Lett.* **101**, 107601 (2008).

33. Nahas, Y. *et al*. Discovery of stable skyrmionic state in ferroelectric nanocomposites. *Nat. Commun.* **6**, 8542 (2015).

Author contributions

A.R.D., J.D.C., R.R. and L.W.M. conceived of the central concepts and designed the experiments. A.R.D., H.L. and M.R.M. conducted the synchrotron and laboratory X-ray diffraction studies. J.D.C. and A.R.D. conducted the scanning probe-based PFM measurements. Z.H. performed and analysed the phase-field simulations. A.K.Y. and M.R.M. synthesized the materials. C.T.N. and S.L.H. performed the TEM-based characterization of the superlattice samples, along with the detailed polarization vector analysis. K.-D.P. and V.K. performed the near- and far-field SHG measurements. A.F. conducted the PEEM measurements. Y.D., Z.C., H.Z. and H.L. conducted the synchrotron nanodiffraction studies. P.A.-P. and J.J. completed the second-principles simulations that were analysed by P.A.-P., P.G.-F., J.Í. and J.J. A.S., M.B.R., L.-Q.C. and D.D.F. contributed to analysis, discussions, and understanding of the data and the development of the manuscript. A.R.D., R.R. and L.W.M. wrote the manuscript. All authors discussed the results and implications of the work and read, edited and commented on the manuscript at all stages.

Additional information

Supplementary information is available in the online version of the paper. Reprints and permissions information is available online at www.nature.com/reprints. Publisher's note: Springer Nature remains neutral with regard to jurisdictional claims in published maps and institutional affiliations. Correspondence and requests for materials should be addressed to L.W.M.

Competing financial interests

The authors declare no competing financial interests.

Methods

Synthesis of superlattices using RHEED-assisted pulsed-laser deposition.
Methods for superlattice synthesis have been performed according to previous
works[26] and are reproduced here for completeness. Superlattices of
$(PbTiO_3)_n/(SrTiO_3)_n$ were grown on 5 nm $SrRuO_3/DyScO_3 (110)_O [(001)_{pc}]$
substrates via pulsed-laser deposition. All depositions were performed at a laser
fluence of $1.5 \, J \, cm^{-2}$ in an on-axis geometry that was found to provide for
stoichiometric transfer of all materials from target to substrate. The $SrRuO_3$ was
grown at a heater temperature of $700\,°C$ and a dynamic oxygen pressure of
50 mtorr. The superlattices were grown at a heater temperature of $630\,°C$ and a
dynamic oxygen pressure of 100 mtorr. The growth was monitored *in situ* using
reflection high-energy electron diffraction (RHEED) and revealed layer-by-layer
growth throughout the growth process (Supplementary Fig. 1), thus enabling
growth of the superlattices with different periodicities while achieving the same
total thickness of 100 nm. RHEED oscillations were monitored for specular spots
along the $[\bar{1}10]_O$ of the $DyScO_3 (110)_O$ substrate. Following growth, the samples
were cooled in 50 torr of oxygen to room temperature to promote oxidation.

Structural characterization using laboratory-based X-ray diffraction.
High-resolution $\theta - 2\theta$ symmetric scans using a Panalytical X'Pert Pro X-ray
diffraction system (Cu source) were used to confirm the superlattice period
achieved via RHEED-controlled growth. The presence of superlattice peaks, as well
as Pendellösung fringes about both the central Bragg and the superlattice peaks (for
example in superlattices with periodicity $n = 6, 10$ (Fig. 1a)), attests to the high
crystallinity of the superlattice structure, and the precise nature and smoothness of
the interfaces in these structures.

Structural characterization using synchrotron X-ray diffraction. Synchrotron
X-ray diffraction studies were employed to study the evolution of structure and
complex phase coexistence in the superlattice structures. The high flux from a
synchrotron source delivered at the Sector 33-BM-C beamline of the Advanced
Photon Source, Argonne National Laboratory was optimal to extract lattice
modulations associated with the nanoscale ferroelectric domains and vortex
structures. A double-crystal monochromator in conjunction with two mirrors was
used to obtain a highly monochromatic beam with negligible higher-order
harmonics. The excellent accuracy of a Huber 4-circle diffractometer in
combination with a PILATUS 100K pixel detector allowed us to obtain
3D-reciprocal space maps (RSMs) with high accuracy and speed. The X-ray
wavelength used for obtaining the RSMs was 0.8 Å (15.5 keV).

Structural characterization using synchrotron X-ray nanodiffraction.
Diffraction microscopy experiments were conducted at Sector 2-ID-D of the
Advanced Photon Source. The 11 keV incident X-rays were focused by a zone plate
to a beam size of ~200 nm and raster scanned over the piezoresponse force
microscopy (PFM)-switched regions. The diffracted X-rays were collected by a
PILATUS 100K pixel array detector. Two regions of interest in reciprocal space
were chosen for imaging: one at the 002-diffraction condition for the a_1/a_2 phase
and the other at the satellite peak position of the vortex phase. In this way, the
structural relationship between the a_1/a_2 phase and the vortex phase could be
measured simultaneously. Wider scans along the out-of-plane 00L direction were
also performed by rotating the sample and detector while maintaining a fixed beam
position outside or inside the PFM-switched regions.

Topography and domain structure characterization. Study of the superlattice
structures was carried out using an atomic force microscope (MFP-3D, Asylum
Research). Dual a.c. resonance tracking PFM was conducted using a conductive
Pt/Ir-coated probe tip (NanoSensor PPP-EFM) to image the domain structures and
complete vectorial PFM studies.

Phase-field simulations. Phase-field simulations were performed to simulate the
polar structure and switching behaviour of the $(PbTiO_3)_{10}/(SrTiO_3)_{10}$ superlattices
grown on $DyScO_3 (110)_O$ substrates. The spontaneous polarization vector ($\mathbf{P}$) is
chosen as the order parameter, governed by the time-dependent Ginsburg–Landau
equations:

$$\frac{\partial P_i(\mathbf{r},t)}{\partial t} = -L \frac{\delta F}{\delta P_i(\mathbf{r},t)} \quad (i=1,2,3) \qquad (1)$$

where t, L and F denote the evolution time step, kinetic coefficient, and total free
energy of the system, respectively. The free energy has contributions from the
Landau, elastic, electric (electrostatic) and gradient energies, that is,

$$F = \int (f_{Landau} + f_{Elastic} + f_{Electric} + f_{Gradient}) \, dV \qquad (2)$$

The detailed expressions of these energies can be found in previous reports[34–39].
A 3D mesh of $200 \times 200 \times 250$ is used, with each grid representing 0.4 nm, the
thickness dimension (from bottom to top) is made up of 30 layers of substrate,

176 layers of film and 22 layers of air. In the film layer, 9 unit cells of $PbTiO_3$, and 9
unit cells of $SrTiO_3$ as well as 1 layer of transition layer in between the $PbTiO_3$ and
$SrTiO_3$ layers are deposited periodically. Periodic boundary conditions are applied
along the in-plane directions, while a superposition method is used in the thickness
dimension[40]. Fixed potential electric boundary conditions are applied where the
electric potentials on the bottom and top are fixed to 0 and the applied bias,
respectively. During the poling process, 15 V is applied on the top electrode. A
mixed elastic boundary condition is used where the displacement on the bottom of
the substrate is zero while the out-of-plane stress on the film top is free. All of the
material constants are adopted from previous literature[37,39–42]. Random noise with
small magnitude ($<0.1 \, \mu C \, cm^{-2}$) is added as the initial nuclei.

Second-principles simulations. Methods for second-principles simulations have
been performed according to previous work[43] and are reproduced here for
completeness. Interactions within the $PbTiO_3$ or $SrTiO_3$ layers are addressed with
previously introduced potentials for the bulk compounds[44]. These potentials give
qualitatively correct descriptions for the lattice dynamical properties and structural
phase transitions of both materials. A simple numerical average was used for
interactions of the ion pairs touching or crossing the interface. Within the
superlattice periodicities studied in this work, the main effects of the stacking are
electrostatic wherein long-range dipole–dipole interactions are governed by the
Born effective charges of the parent compounds and a bare electronic dielectric
constant ε_∞ is taken as a weighted average (with weights reflecting the composition
of the superlattice) of the first-principles results for $PbTiO_3$ ($\varepsilon_\infty^{PbTiO_3} = 8.5 \, \varepsilon_0$) and
$SrTiO_3$ ($\varepsilon_\infty^{SrTiO_3} = 6.2 \, \varepsilon_0$). To preserve the electrostatic energy within each material
as close as possible to the bulk parent compounds, the Born effective charge tensors
of the inner atoms were rescaled by $\sqrt{\varepsilon_\infty}/\varepsilon_\infty^{ABO_3}$ (where ABO_3 stands for $PbTiO_3$ or
$SrTiO_3$ depending on the layer) and, as noted in equation (23) of ref. 44, the
dipole–dipole interactions were maintained to be the same as bulk. For atoms
touching the interfaces, the Born effective charge tensors were left untouched.
In-plane lattice constants of $a = b = 3.901$ Å were assumed. An external expansive
hydrostatic pressure of -11.2 GPa was imposed to counter underestimation of the
local density approximation of the cubic-lattice constant that was taken as the
reference structure for the fitting of the second-principles parameters. Such
approximations and adjustments allow for the construction of models for
superlattices of arbitrary n stacking. Simulations applied periodically repeated
supercells that containing $2n \times 2n$ elemental perovskite units in-plane, an one full
supercell period in the out-of-plane direction.

Local polarizations were computed within a linear approximation of the
product of the Born effective charge tensor times the atomic displacements from
the reference structure positions divided by the volume of the unit cell. The effect
of external electric fields was incorporated in the effective Hamiltonian simulation
by including the leading coupling term between the field and the local dipoles. The
models were solved via Monte Carlo simulations comprising 10,000 thermalization
sweeps followed by 40,000 sweeps to compute thermal averages. If the Metropolis
Monte Carlo samplings are performed at low temperature, then only random
configurations along the Markov chains that produce a lowering in the energy are
accepted, so this procedure can be used as an equivalent to structural relaxations to
find the ground state.

Conventional and scanning transmission electron microscopy. Methods for
TEM-based studies have been performed according to previous work[26] and are
reproduced here for completeness. Samples for TEM studies were produced via
mechanical polishing on an Allied High Tech Multiprep. Cross-sectional samples
were polished at a 0.5° wedge, and planar samples with a flat polish. Following
polishing, the samples were Ar-ion milled using a Gatan Precision Ion Milling
System from a starting energy of 4 keV to a final cleaning energy of 200 eV.

Scanning TEM was performed on a Cs-corrected TEAM0.5 FEI Titan
microscope at 300 kV using a high-angle annular detector resulting in 'Z-contrast'
images. Raster distortion was minimized using a pair of HR-STEM images of the
same region taken with orthogonal scan orientations. These orthogonal scan
orientation images were used to calculate a corrected 'pre-distortion' image to
minimize the slow scan axis[45]. Mapping and extraction of the polar atomic
displacements ($\mathbf{P}_{PD}$) was performed on the corrected HR-STEM for high-angle
annular dark-field images using local A- and B-site sublattice offset
measurements[46]. This process is based on the fact that for many displacive
perovskite ferroelectrics the electric dipole moment is manifested by relative shifts
of the cations, as is the case for $PbTiO_3$, and this offset can be used to infer the
polarization ($\mathbf{P}$). This is helpful since the anions (oxygen) have relatively weak
electron scattering resulting in low signal-to-noise ratio, especially for high-angle
annular dark-field images, limiting the impact they can have on characterizing the
electric dipole. In bulk $PbTiO_3$ at room temperature, the Ti and O ions are shifted
by 16.2 pm and 47–49 pm in the direction opposite to the polarization, respectively,
relative to the Pb lattice[47]. In turn, we can use the Ti ions to infer the offset of the
Ti-centred oxygen octahedra, which can be used to determine the electric dipole.
Displacement vectors ($\mathbf{P}_{PD}$) corresponding to local offsets between the A- and

B-site sublattices were calculated in the following three steps. First, the atomic positions were determined by fitting each atom site in the image to four-parameter, spherical Gaussians using a trust-region algorithm in Matlab. Such fits were performed simultaneously for five-atom clusters of the *B*-site-centred perovskite unit cell. Second, the displacement for each atom is then calculated as the difference between its atom position and the mean position (that is, the centre of mass) of the surrounding four opposite-type cations. Using a pseudocubic grid indexing (wherein *A*-sites define the grid) and defining the cross-section image to lie in the *x*–*z* Cartesian plane ($x = [100]_{pc}$, $z = [001]_{pc}$), for an atom at grid position i, j this corresponds to mean neighbour positions (MNPs) of:

$$MNPx_{ij} = 1/4[x_{i-0.5,j-0.5} + x_{i-0.5,j+0.5} + x_{i+0.5,j+0.5} + x_{i+0.5,j-0.5}]$$
$$MNPz_{ij} = 1/4[z_{i-0.5,j-0.5} + z_{i-0.5,j+0.5} + z_{i+0.5,j+0.5} + z_{i+0.5,j-0.5}]$$

Finally, the polar displacement vector is defined with reversed order for *A*- and *B*-site-centred atoms to maintain a consistent displacement vector sign (otherwise it would alternate directions):

$$\mathbf{P}_{PD,ij\,A\text{-site}} = (x_{ij} - MNPx_{ij})\hat{x} + (z_{ij} - MNPz_{ij})\hat{z}$$
$$\mathbf{P}_{PD,ij\,B\text{-site}} = (MNPx_{ij} - x_{ij})\hat{x} + (MNPz_{ij} - z_{ij})\hat{z}$$

This convention defines a displacement vector direction nominally parallel to the full electrical polarization of the bulk crystal structure.

The curl vector (or vorticity) of the displacement vector field $\mathbf{P}_{PD}$ in the TEM plane is the *y* component of $\nabla \times \mathbf{P}_{PD}$ or $((\partial P_{PD,z}/\partial x) - (\partial P_{PD,x}/\partial z))\hat{y}$ (again the TEM image is defined as the *x*–*z* plane, *y* is the direction of the electron beam). The polarization gradient terms $\partial P_{PD,z}/\partial x$ and $\partial P_{PD,x}/\partial z$ were calculated by a weighted least-squares fit of a two-variable (*x* and *z*) first-order polynomial to $\mathbf{P}_{PD,x}$ and $\mathbf{P}_{PD,z}$ at each atom site with a fit area extending to 12 surrounding atoms. Said a different way, the local $\mathbf{P}_{PD,x}$ and $\mathbf{P}_{PD,z}$ values were fitted as a plane, and the derivatives are taken as the *x* and *z* slopes of the plane. A Gaussian function with a σ of the mean grid spacing was used as the weighting function; that is, the central atom was given a weight of 1 and decreased to a weight of ~0.1 for the most distant of the 12 neighbour atoms considered. The polynomial fit was used as a smoothing function for the vector fields displayed in the figures, effectively smoothing the first derivative, and the gradients input into the curl equation.

Photoemission electron microscopy (PEEM)-based X-ray linear dichroism.
X-ray linear dichroism in the near-edge X-ray absorption fine structure senses the local anisotropy of the electron charge cloud, and is sensitive to the local ferroelectric polarization axis. PEEM images and spectra were taken at the Ti L_3 edge using s- (along [100]) and p- (30° from [001]) polarized X-rays. Vortex and ferroelectric regions are distinguished in X-ray linear dichroism PEEM images mainly by their different [100] polarization components.

Second-harmonic generation (SHG) and SHG nano-imaging. A typical reflection mode geometry was used the far-field SHG anisotropy measurement, with combinations of input and output polarizations selected by an achromatic half-wave plate and a polarizer to probe specific tensor components. The backscattered SHG intensity was then measured while keeping the polarization optics stationary and rotating the sample. For near-field SHG nano-imaging, a shear-force atomic force microscopy-based scattering scanning near-field optical microscopy set-up was used in a tilted tip geometry as described previously[48,49]. The Au tip was illuminated from the top by broadband ~10 fs pulses derived from

a Ti:sapphire oscillator (Femtolasers, 800 nm centre wavelength, 78 MHz repetition rate), with tip-parallel polarization and average incident power of 3 mW. The tip-enhanced SHG signals were collected by a microscope objective (100×, NA = 0.8) in the back-reflection geometry and detected with a spectrometer and a CCD (charge-coupled device; Princeton Instruments).

Data availability. All relevant data are available from the authors, and/or are included with the manuscript as source data or Supplementary Information including that in Figs 1–5 and Supplementary Figs 1–13.

References

34. Chen, L. Q. Phase-field method of phase transitions/domain structures in ferroelectric thin films: a review. *J. Am. Ceram. Soc.* **91,** 1835–1844 (2008).
35. Xue, F. *et al.* Phase field simulations of ferroelectrics domain structures in PbZr$_x$Ti$_{1-x}$O$_3$ bilayers. *Acta Mater.* **61,** 2909–2918 (2013).
36. Wang, J. J., Ma, X. Q., Li, Q., Britson, J. & Chen, L. Q. Phase transitions and domain structures of ferroelectric nanoparticles: phase field model incorporating strong elastic and dielectric inhomogeneity. *Acta Mater.* **61,** 7591–7603 (2013).
37. Li, Y. L., Hu, S. Y., Liu, Z. K. & Chen, L. Q. Effect of substrate constraint on the stability and evolution of ferroelectric domain structures in thin films. *Acta. Mater.* **50,** 395–411 (2002).
38. Li, Y. L., Hu, S. Y., Liu, Z. K. & Chen, L. Q. Effect of electrical boundary conditions on ferroelectric domain structures in thin films. *Appl. Phys. Lett.* **81,** 427–429 (2002).
39. Chen, L. Q. & Shen, J. Applications of semi-implicit Fourier spectral method to phase field equations. *Comput. Phys. Commun.* **108,** 147–158 (1998).
40. Haun, M. J., Furman, E., Jiang, S. J., Mckinstry, H. A. & Cross, L. E. Thermodynamic theory of PbTiO$_3$. *J. Appl. Phys.* **62,** 3331–3338 (1987).
41. Sheng, G. *et al.* A modified Landau–Devonshire thermodynamic potential for strontium titanate. *Appl. Phys. Lett.* **96,** 232902 (2010).
42. Chen, Z. H., Damodaran, A. R., Xu, R., Lee, S. & Martin, L. W. Effect of 'symmetry mismatch' on the domain structure of rhombohedral BiFeO$_3$ thin films. *Appl. Phys. Lett.* **104,** 182908 (2014).
43. Zubko, P. *et al.* Negative capacitance in multidomain ferroelectric superlattices. *Nature* **534,** 524–528 (2016).
44. Wojde, J. C., Hermet, P., Ljungberg, M. P., Ghosez, P. & Iniguez, J. First-principles model potentials for lattice-dynamical studies: general methodology and example of application to ferroic perovskite oxides. *J. Phys. Condens. Matter* **25,** 305401 (2013).
45. Ophus, C., Nelson, C. T. & Ciston, J. Correcting nonlinear drift distortion of scanning probe microscopy from image pairs with orthogonal scan directions. *Ultramicroscopy* **162,** 1–9 (2016).
46. Nelson, C. T. *et al.* Spontaneous vortex nanodomain arrays at ferroelectric heterointerfaces. *Nano Lett.* **11,** 828–834 (2011).
47. Glazer, A. M. & Mabud, S. A. Powder profile refinement of lead zirconium titanate at several temperatures. II. PbTiO$_3$. *Acta Crystallogr. B* **34,** 1065–1070 (1978).
48. Neacsu, C. C., van Aken, B. B., Fiebig, M. & Raschke, M. B. Second-harmonic near-field imaging of ferroelectric domain structure of YMnO$_3$. *Phys. Rev. B* **79,** 100107 (2009).
49. Park, K. D. *et al.* Hybrid tip-enhanced nanospectroscopy and nanoimaging of monolayer WSe$_2$ with local strain control. *Nano Lett.* **16,** 2621–2627 (2016).